Page Proof Instructions and Queries

Greetings, and thank you for publishing with SAGE. We have prepared this page for your review. Please respond to each of the below queries by digitally marking this PDF using Adobe Reader (free at https://get.adobe.com/reader).

Please use *only* the circled tools to indicate your requests and responses, as edits via other tools/methods are not compatible with our software. To ask a question or request a formatting change (such as italics), please click the ⟲ tool and then choose "Text Callout." To access the necessary tools, choose "Comment" from the right-side menu.
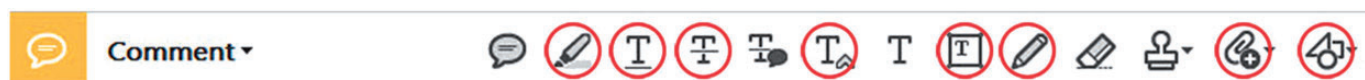
No.	Query
	Please confirm that all author information, including names, affiliations, sequence, and contact details, is correct.
	Please review the entire document for typographical errors, mathematical errors, and any other necessary corrections; check headings, tables, and figures.
	Please confirm that the Funding and Conflict of Interest statements are accurate.
	Please ensure that you have obtained and enclosed all necessary permissions for the reproduction of artistic works, (e.g. illustrations, photographs, charts, maps, other visual material, etc.) not owned by yourself. Please refer to your publishing agreement for further information.
	Please note that this proof represents your final opportunity to review your article prior to publication, so please do send all of your changes now.
AQ: 1	Please provide the expansion for DLR.
AQ: 2	Please confirm whether Table 2 is OK as set.
AQ: 3	Please provide the author group in Refs. 22 and 23.
AQ: 4	Note that Refs. 21–24 have been renumbered in order to maintain sequential order in the text. Please check.

All queries have been checked carefully. Please see the following notes for any revision.

Performance improvement of transonic centrifugal compressors by optimization of complex three-dimensional features

Xiao He and Xinqian Zheng

Abstract
Transonic centrifugal compressors with high efficiency and wide stable flow range are required in modern gas turbine engines. Blade design with complex three-dimensional features is one of the promising methods to further improve the performance of such cases. Aiming to increase the efficiency while maintaining similar level of the stable flow range, this article investigates aerodynamic potentials of complex three-dimensional features in a transonic centrifugal compressor by multi-point and multi-objective optimizations, in which the camber curves, the sweep feature, and the lean feature have been optimized. During the first round of optimizations, the aforementioned three groups of variables are optimized individually, and their sensitivities to the performance have been analyzed. When optimizing the camber curves, the best result shows an end-bend feature at the front of the hub section, and the efficiency is improved by 1.0% due to the lowered shock strength. When optimizing the sweep feature, the best result presents an S-shape leading edge and a forward sweep feature. The efficiency is increased by 0.5% because of the reduced wake region. The optimized lean feature only improves the efficiency by 0.2%, which shows its relatively low potential. The final round of optimizations couples both the camber curves and the sweep feature, and the best geometry combines both the end-bend and S-shape leading edge patterns. The peak efficiency and the choke mass flow rate have been increased by 2.2% and 8.1%, respectively, which is owing to the combination of the lowered shock strength by optimized camber curves and the reduced wake region by optimized sweep feature. The result indicates significant potential of complex three-dimensional features to improve the performance of transonic centrifugal compressors.

Keywords
Multi-objective optimization, transonic centrifugal compressor, sweep, lean, end-bend

Introduction

Centrifugal compressors are extensively applied to gas turbine engines and turbochargers. In the aviation industry, transonic centrifugal compressors with high pressure ratios are especially preferred for reduction of manufacturing cost and engine weight.[1] However, due to the rapid drop of stable flow range (SFR)[2] and efficiency[3] with increasing pressure ratio, the application of such compressors is still limited. For the past 20 years, plenty of researches have been conducted on designing high performance transonic centrifugal compressors[4] as well as understanding their flow phenomena under transonic inlet conditions.[5] It is generally found that strong shocks will exist on the shroud section of the impeller, and the interaction between the shock wave, the boundary layer, and the tip leakage vortex will deteriorate the complex flow field and the performance of transonic centrifugal impellers.

To reach the demanding performance goal of transonic centrifugal compressors, one of the most promising methods is to apply complex three-dimensional features to impellers. There are three groups of key variables defining the complex three-dimensional features: the shape of the blade camber curves, the sweep feature, and the lean feature.

The shape of the blade camber curves near the leading edge is crucial to control shock waves and flow separations. According to the theoretical deduction from Lohmberg et al.,[6] the shroud camber curve with low curvature at the tip near the leading edge is

Turbomachinery Laboratory, State Key Laboratory of Automotive Safety and Energy, Tsinghua University, Beijing, China

Corresponding author:
Xinqian Zheng, Turbomachinery Laboratory, State Key Laboratory of Automotive Safety and Energy, Tsinghua University, Beijing 100084, China.
Email: zhengxq@tsinghua.edu.cn

advantageous to decrease the pre-shock Mach number, and thus the related loss. Eisenlohr et al.[7] demonstrated that an adjustment on the front part of hub camber curve could eliminate the high incidence and decrease the corresponding loss. By re-cambering at the front part of both hub and shroud sections together, it was demonstrated in multi-stage axial compressors that the overall efficiency could be improved by 0.4%, where the blade near endwall regions presents an end-bend feature.[8] However for centrifugal compressors, limited researches on exploring the aerodynamic potential of applying end-bend feature have been reported.

Sweep is a degree of freedom of the blade stacking style. When the shroud section of the blade extends upstream in the chord line direction (or axial direction), it is defined as forward sweep. The opposite is regarded as aft-sweep. For axial cases, swept blade design has been extensively studied in compressor rotors[9] and fans.[10] It is generally found that the stall margin was improved by forward sweep, and most forward swept cases showed better efficiency than that of the unswept or the aft-swept ones. Mechanisms of sweep on the flow field can be summarized as redistributing the front loading, controlling the shock structure, and controlling the radial migration of high-loss fluid. For centrifugal cases, swept blades have relatively seldom been reported. Hazby and Xu[11] confirmed the aforementioned flow mechanisms of sweep in a turbocharger impeller case. However, the aerodynamic potential of optimizing sweep feature remains uncertain.

Lean is also a degree of freedom of the blade stacking style. It is defined as moving the shroud section of the blade relative to the tangential direction or perpendicular to the chord direction. When the moving direction is in consistence with the rotating direction, it is defined as positive lean. Otherwise it is regarded as negative lean. For axial cases, blade lean design has been widely applied in axial compressors and turbines, and its aerodynamic effects on axial turbomachines were reviewed by Denton and Xu.[12] The direct effect of blade lean is to introduce a radial blade force, which leads to the change in streamline curvature and the change in radial pressure gradient. The ratio of these two changes is deduced to be positively related to the aspect ratio. For high aspect ratio axial cases, the induced lean feature mainly affects the streamline curvature and its application is to control the root reaction.[13] While for low aspect ratio axial cases, the induced lean feature mainly changes the radial pressure gradient and it is adopted to control the spanwise loading distribution.[14] For centrifugal cases, relatively less researches about blade lean have been reported. He and Zheng[15] investigated mechanisms of lean feature on the performance of a transonic centrifugal compressor. Although little efficiency increment was obtained, lean showed the potential to control the shock structure and suppress the wake region.

Therefore, the aerodynamic potential of optimizing lean feature is still worth digging.

With the rapid development of optimization methods, evaluation of the aerodynamic potential by complex three-dimensional blade design is now technically possible. One of the most effective optimization methods is the combination of a genetic algorithm, an artificial neural network functioning as the surrogate model, and a computational fluid dynamics (CFD) solver.[16] There are plenty of applications of this method to both axial and radial compressors in previous research. Okui et al.[17] adopted the method to optimize the sweep and the chord length of an axial rotor, and the efficiency was successfully increased by 0.7% without losing the surge margin. Sweep and lean of the stators of a five-stage axial compressor were optimized by Lu et al.[18] through the same method, and an increase of 0.22% in the efficiency of the whole compressor was obtained when sweep and lean were optimized in the first stator stage. The method with a finite element stress analysis solver was applied by Verstraete et al.,[19] and stresses of the investigated centrifugal compressor were successfully reduced with only a small drop in efficiency. Ju et al.[20] performed a multi-objective optimization through this method on an impeller, in which the operating range has been extended with maintained peak efficiency. In general, this method is effective and mature and it is therefore chosen in the current study.

The motivation of this article is to evaluate the aerodynamic potential of different geometric variable groups of complex three-dimensional features, which is crucial for future designs of high performance transonic centrifugal compressors. A multi-point and multi-objective optimization has been performed on the complex three-dimensional features design of a transonic centrifugal compressor. The optimization method includes a genetic algorithm, an artificial neural network, and a CFD solver. The blade camber curves, the sweep feature, and the lean feature have been optimized to obtain the three-dimensional design. In the first round of optimizations, three groups of variables have been optimized individually in order to analyze the sensitivity of different variable groups. In the second round, the most potential variable groups have been considered together in the optimization to obtain the final optimized design. Comparisons between the datum and the optimized cases in geometry and performances have been made. The aerodynamic mechanisms of optimized cases on performances and flow fields have been discussed in detail.

Case description

The investigated transonic centrifugal impeller SRV2-O is an open test case from DLR, whose specification is given in Table 1. **[AQ1]** The three-dimensional geometry of the impeller blade is generated by a linear connection between points of hub and shroud sections, which allows it to be manufactured by flank milling.

The leading edges of main blades and splitters are radial stacked, and the trailing edges of all blades are axial stacked. A vaneless diffuser is attached to the impeller downstream. The open test case has been subjected to both rig tests and laser-two-focus measurements, which will be referred to in the validation of the numerical method.

Optimization method

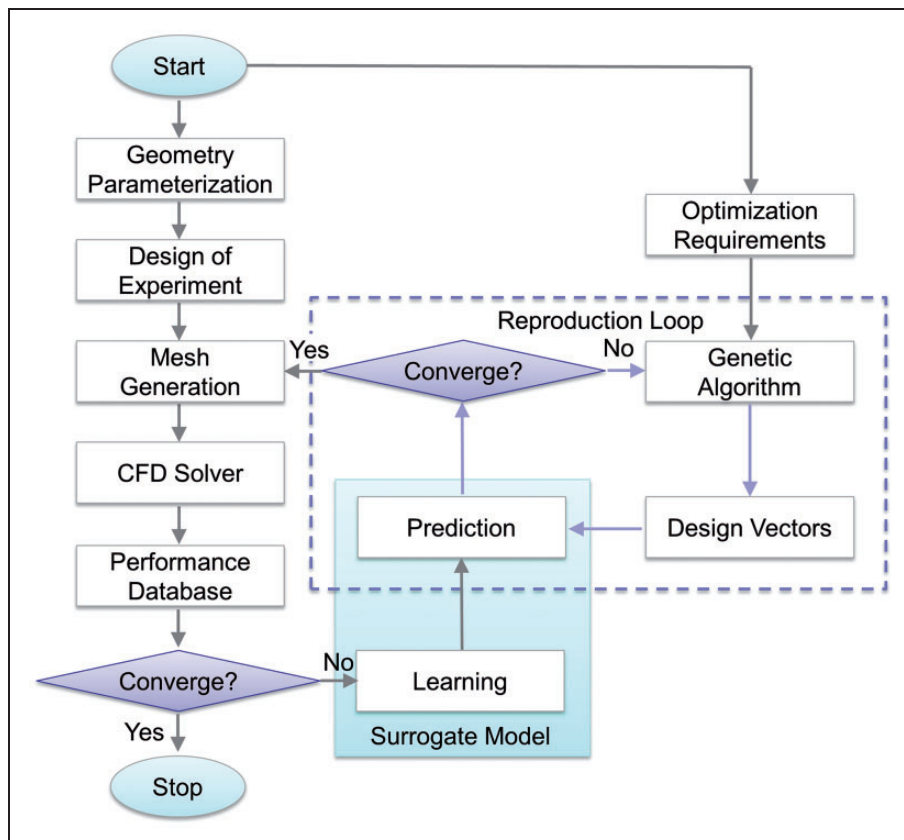The optimization kernel adopted in this article is Design3D[21] that combines a genetic algorithm, an artificial neural network, and a CFD solver. It begins with the geometry parameterization that provides the design variables. The design of experiment is then carried out to generate a representative initial sample database of design variables, whose aerodynamic performances will be later predicted by the CFD solver. Based on the knowledge of the performance database, the artificial neural network is constructed as the surrogate model of the CFD solver to give a quicker performance prediction. During each reproduction loops, the performances of the generated population by the genetic algorithm are predicted by the artificial neural network. After several generations of competence and selection, the reproduction loop converges, and the performance of the best result will be verified by the CFD solver and be updated in the database. A new artificial neural network is then built based on the updated database, and the next iteration of the optimization begins. The flowchart of the optimization process is given in Figure 1.

Geometry parameterization

The geometry of the impeller is parameterized by the meridional contours of hub and casing, blade camber curves at hub and shroud sections, blade thickness distribution normal to the camber curve, leading

Table 1. Design specification of SRV2-O impeller.[7]

Parameters	Symbols	Values
Shaft speed	n	50,000 r/min
Mass flow rate	m	2.55 kg/s
Pressure ratio	π_{12}	6.1
Number of blades	Z	$13 + 13$
Leading edge hub radius	r_{1h}	30 mm
Leading edge tip radius	r_{1t}	78 mm
Blade angle leading edge tip	β_{1t}	26.5 deg
Impeller tip radius	r_2	112 mm
Exit blade height	b_2	10.2 mm
Blade angle trailing edge	β_2	52 deg

Figure 1. Flowchart of the integrated optimization design system.

edge and trailing edge traces, and the number of blades. The camber curve of the main blade is truncated to define the splitters with respect to the constant relative meridional position of the splitter leading edge. Therefore, when modifications are made on main blades, splitters will be changed in similar fashion.

Camber curves of the main blade are constructed in the (m', θ) plane. Each of the curves is defined by a Bezier curve with eight control points, whose meridional distribution follows the stretching factor of 1.1 from the leading edge to the trailing edge. The theta angle of front three control points at hub (T1H to T3H) and shroud (T1S to T3S) sections are chosen as design variables, while others are remained unchanged. Schematics of camber curves definition is illustrated in Figure 2(a) and (b).

Sweep is the feature that describes the leading edge shape in the meridional direction. It is defined by a Bezier curve with four control points, as illustrated in Figure 2(c). The axial position of the top control point is often quantitatively defined by the sweep angle

(SA), which is the angle between the radial direction and the leading edge direction that goes through the top and the bottom point of the leading edge. A positive value of SA represents forward sweep and the opposite is aft-sweep. The curved shape of the leading edge is determined by the other three control points in the middle. They are uniformly distributed along the leading edge direction, and their distances perpendicular away from this direction are variables namely S1 to S3. It should be noted that the sweep definition is independent of the unchanged trailing edge radius, and thus the application of sweep will change the blade chord length at all spans. In this study, the SA as well as S1, S2, and S3 are chosen as design variables to define the sweep feature.

Lean is the feature that describes the leading edge shape in the tangential direction. It is also defined by a Bezier curve with four control points, as illustrated in Figure 2(d). When the top control point L4 moves to the rotating direction or has a positive theta angle in this case, it is generally regarded as positive lean. The middle control points determine the curved shape of
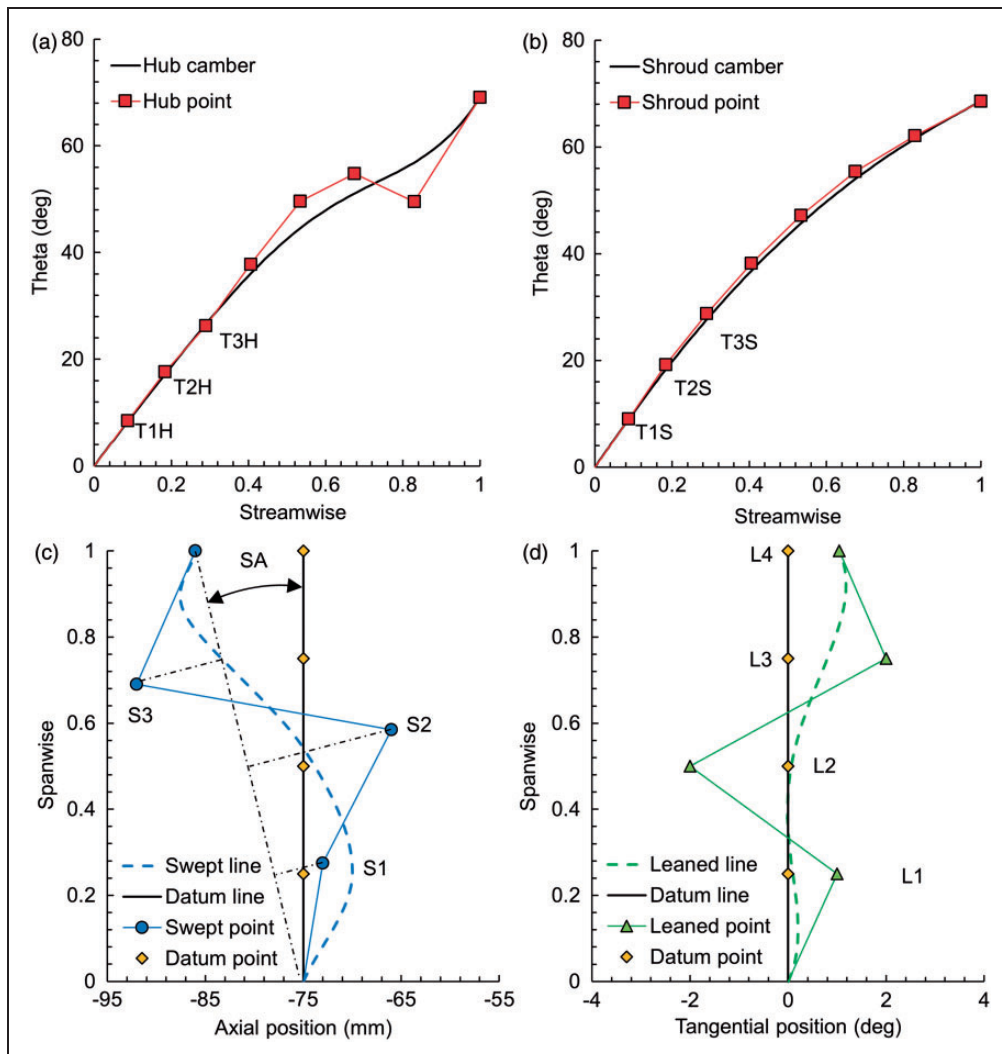

Figure 2. Schematic of variables definition: (a) hub camber curve, (b) shroud camber curve, (c) sweep, and (d) lean.

the leading edge. They are uniformly distributed along the spanwise direction, and their tangential positions are variables namely L1 to L3. It should be noted that lean can be viewed as moving the blade profiles at different spans relative to the tangential direction. Therefore, lean is independent of the blade profiles, and it changes the geometry not only in the front part but also in the rear part of the impeller. In this study, L1, L2, L3, and L4 are chosen as design variables to define the lean feature.

Variation range of all design variables are given in Table 2, where the values of S1 to S3 are normalized by the distance between the top and the bottom point of the leading edge. Because a wider variation range of each variable group will result in too many invalid samples that are too odd in geometry to be meshed, the current range is therefore considered appropriate for optimization.

Initial database sampling method

To explore the variable design space efficiently and effectively, an initial database with a limited number of representative samples is needed. One of the most effective sampling methods for multidimensional

The current form of Table 2. is OK for publication

Table 2. Variation range of design variables. [AQ2]

Variables		Range
Theta	T1H–T3H	±5°
	T1S–T3S	
Sweep	SA	±10°
	S1–S3	±2%
Lean	L1–L4	±2°

design variables is Latin hypercube sampling. When sampling M sample points in an N-dimensional variable space, the method divides the design range of each variable into M equally probable intervals, and sample points are then distributed in the way that each interval of all variables only contains one sample point. Through this method, about 50 valid samples are obtained as the initial database during each optimization rounds, which is over five times of the number of design variables.

Mesh generation

A multi-block structured grid is built to mesh the impeller, as shown in Figure 3. For the O4H topology of the impeller, the final grid of the datum compressor has 1.4 million cells for single pitch, which consists of 117, 69, and 43 nodes in the streamwise, spanwise, and pitchwise direction, respectively. The tip clearances of all blades are linearly varying from 0.5 mm at the impeller inlet to 0.3 mm at the impeller exit. To predict a boundary layer resolution sufficiently fine for the Spalart–Allamaras model, a value of 0.005 mm is found appropriate for the first layer wall distance of the near-wall grid. Because the scalar averaged y^+ value is around 3.6, most part of the near-wall grid locates within the viscous sublayer that has an upper y^+ bound of 5. For other parts of the near-wall grid, the local maximum value of y^+ is kept below 10, which is an acceptable approximation for design conditions as suggested by the solver provider.[22] The same mesh topology and mesh size have been adopted during optimization loops.

The accuracy of the simulation results is related to the grid size. Seven different mesh sizes have been investigated, whose number of nodes varies from 0.9
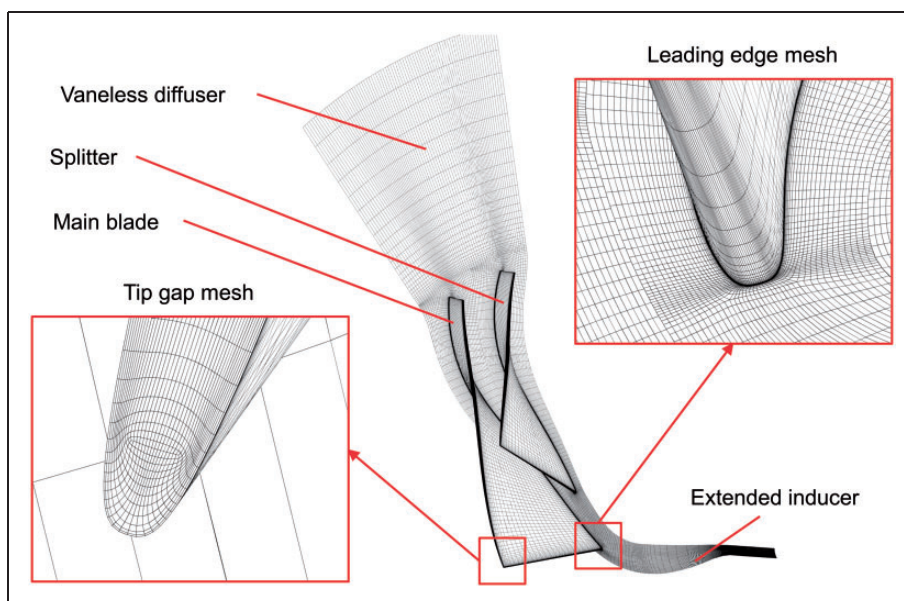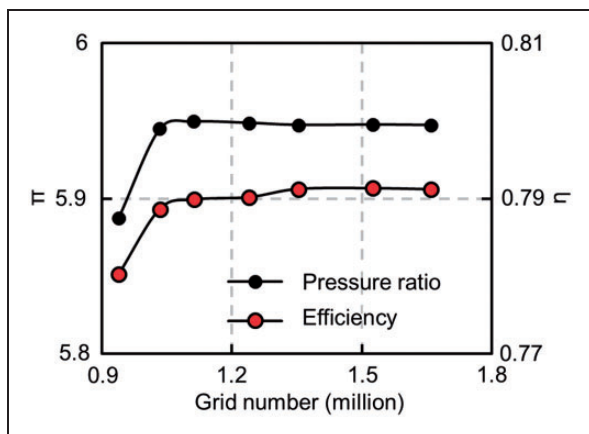

Figure 3. Created computational mesh in detail.

million up to 1.6 million. The resulting performance of all meshes near peak efficiency condition at design speed is plotted in Figure 4, where all cases share the same mass flow rate. It is illustrated that the CFD simulation produces consistent results when the mesh nodes surpass 1.1 million. Therefore, the final grid with 1.4 million nodes is considered to be independent of the mesh resolution.

CFD solver

The simulation by CFD is done with the solver EURANUS[22] based on a three-dimensional steady, compressible, finite volume scheme to solve the Reynolds-averaged Navier–Stokes equations in the conservative formulation. To receive a credible viscosity resolution, spatial discretization is achieved with modified Jameson central difference scheme. The fourth-order Runge–Kutta scheme is applied for temporal discretization. The convergence of the solver is accelerated by the multigrid procedure. After evaluation of several turbulence models in Table 3, the Spalart–Allamaras one-equation model[23] has been adopted because its predicted performances are closest to experiments and the computation time needed is the least.

Total pressure, total temperature, and velocity components are imposed at the inlet, and an average static pressure is imposed at the exit. The blades and casing surface are defined as the rotational nonslip solid boundary and the static nonslip solid boundary, respectively. For each rotation speed, the initial solution of the first simulation case is defined by estimation of velocity components, static pressure, and temperature for the whole domain. The former converged result is then used as the initial solution for the next case with higher backpressure. The step rise in backpressure at the near-surge condition is kept as 1 kPa. If no signs of numerical instabilities occurred after 10,000 iterations, the solution is considered to have reached convergence. The convergence history of the CFD simulation at peak efficiency condition of the datum compressor has been illustrated in Figure 5.

Figure 6 compares the predicted performance map with experiment results.[24] The satisfactory agreement is obtained at low speeds. However, when the speed

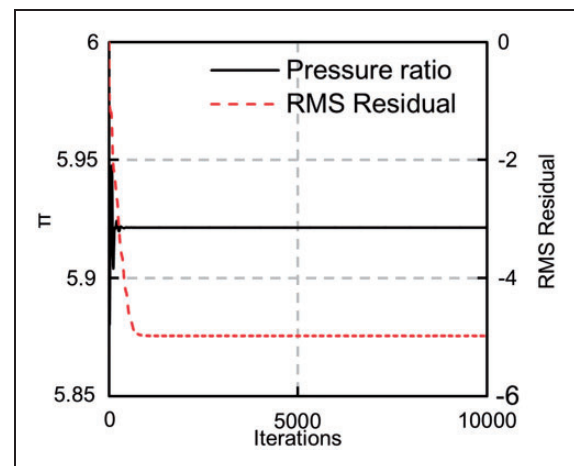**Figure 5.** Convergence history of the CFD simulation.

Figure 4. Performance near peak efficiency condition at design speed with different grid size.

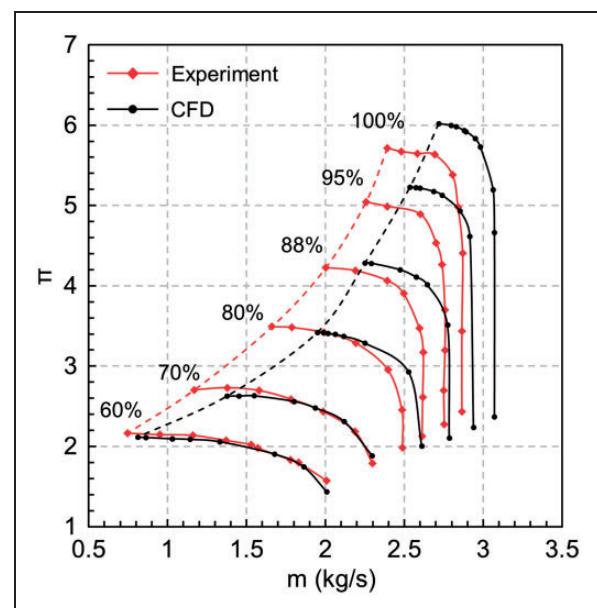**Table 3.** Effect of turbulence models on performance prediction.

Models	Equation numbers	π_{14} (m/m$_c$ = 0.89)	m$_c$ (kg/s)
Experiment	–	5.65	2.87
SA	1	6.01	3.07
k-ε	2	6.03	3.07
SST	2	6.16	3.08

Figure 6. Comparison of performance map between experiment and CFD result.

increases, the predicted choking mass flow rate and the pressure ratio are gradually growing higher than that of the experiment results where such differences peak at design speed by +7.2% and +5.3%, respectively. The inconsistency not only occurs in the current research, but was also reported by former researchers.[25,26] It is also noticed in Figure 6 that inconsistency also exists for the surge point prediction. In this steady case, the surge point is defined as the converged point with the highest backpressure. However, it is misleading to deduce the time-dependent system oscillations from numerical steady-state instabilities. It can be viewed as a systematic error due to the limitation of the steady simulations.

Except for the possible geometric difference between the experiment and the simulation, some of the factors that may lead to the inconsistency between the experiment and CFD at nonsurge conditions are listed as follows.

1. Fillet at the root of blades are ignored in simulations. According to the results from Yi et al.,[25] a fillet radius of 6.3% of the inlet blade height in the same case would lead to a −1.4% change in the predicted pressure ratio.
2. Applications of different turbulence models are expected to have different results in global performance. Referring to the former part of turbulence models evaluation, applications of different turbulence models resulted in a change in pressure ratio as much as +2.6% compared to the SA model. Mangani et al.[26] applied the AWT model on the same compressor, and a −0.9% change in pressure ratio compared to the current results by the SA model was obtained.
3. The blade deformation is ignored in simulations. Under running conditions, the blade of centrifugal compressors tends to deform with a lower radial tip gap size and a positive lean feature. The larger the operating speed, the stronger its effects on the performance. Hazby et al.[27] evaluated the deformation effects in a transonic mixed flow compressor, and the pressure ratio of the deformed case was increased by +1.4% mainly due to the decreased tip gap size.
4. The backside cavity is not considered in simulations. Sun et al.[28] found that the pressure ratio was changed by −0.9% when considering the backside cavity and a leakage flow rate of about 1% of the design mass flow. At high pressure ratio conditions, the leakage flow rate is expected to increase and thus its effects on the performance are expected to be more severe.
5. The internal heat transfer from the hot downstream part to the cool upstream part through the solid impeller and casing is ignored in simulations. As reported by Gu et al.,[29] the predicted pressure ratio of a centrifugal compressor was varied by −1.3% after considering internal heat transfer. Similar works are still needed in high pressure ratio centrifugal compressors in future research.
6. The unsteady effect is missed in steady simulations. Benichou and Trebinjac[30] compared the steady and unsteady simulation results of a transonic centrifugal compressor with a vaned diffuser. It was found that the pressure ratio predicted by unsteady simulations is slightly changed by −1.4% at peak efficiency condition, and the internal flow structure of the vaned diffuser is significantly different to that of the steady case. The reported differences are mainly due to the application of the mixing plane model between the rotating impeller and the stationary vaned diffuser in steady simulations. For the current case with a vaneless diffuser, since no mixing plane model is needed in steady simulations, the unsteady effect on predicting the pressure ratio is believed to be less significant.

To sum up the above discussion, influence of above factors on predicting the pressure ratio is summarized in Table 4. The high fidelity CFD simulation on high pressure ratio transonic centrifugal compressors is still an open topic for future research, and it is meaningful to evaluate effects of above factors in a same compressor. For the current research, the difference between experiments and CFD can be regarded as the systematic error due to the simplification of the numerical model, which can be avoided by comparing performances between the datum and the optimized case with valid mechanisms from the flow field.

To validate the capability of the numerical method of predicting the detailed flow field, comparison has been made between the CFD and the measurement results by Krain.[24] The compared working condition is $m/m_c = 0.89$ at design speed, where a strong shock wave occurs at the leading edge of the main blade. Figure 7 presents the comparison of relative Mach number near the inlet and the exit, respectively. It is illustrated in Figure 7(a) that the shock position and the shock strength have been well captured at the tip section. In Figure 7(b), the jet-wake pattern in both passages has been well predicted as well. The numerical method is therefore considered capable of

Table 4. Influence of factors on predicting the pressure ratio.

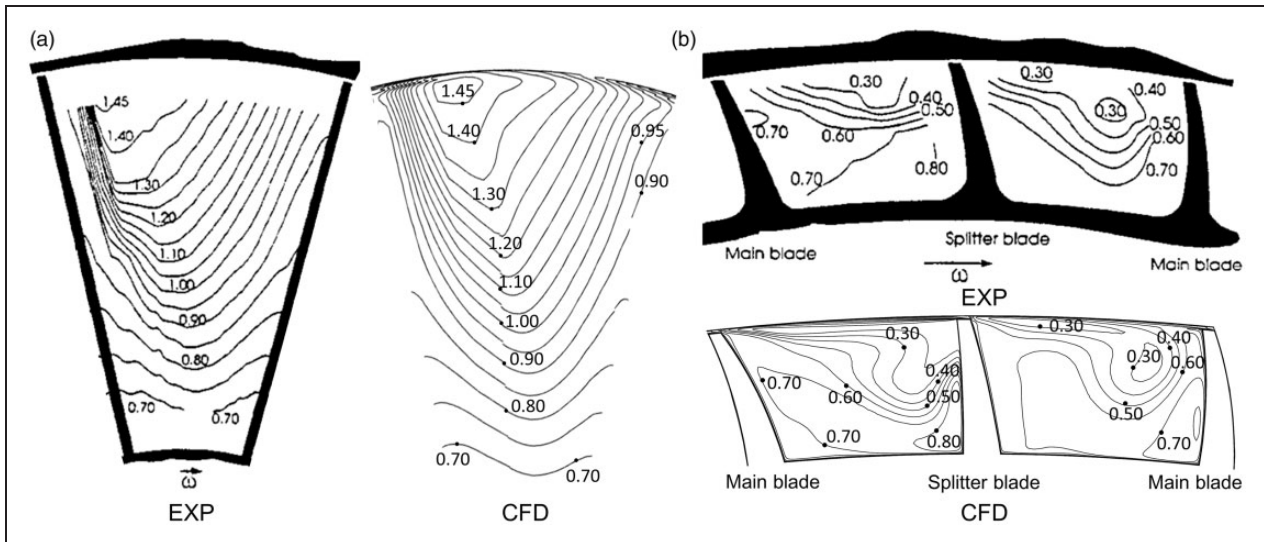| Factors	$\triangle\pi/\pi_d$	π_d
Fillet[25]	−1.4%	5.7
Turbulence model[26]	−0.9% to +2.6%	5.7
Blade deformation[27]	+1.4%	2.8
Backside cavity[28]	−0.9%	4.4
Internal heat transfer[29]	−1.3%	3.6
Unsteady effect[30]	−1.4%	—

Figure 7. Comparison of relative Mach number of SRV2-O between experiments and CFD near (a) the inlet and (b) the exit.

predicting the flow details, especially for the shock wave and jet-wake pattern.

Surrogate model

Because the genetic algorithm demands tremendous amount of computation resources for the required population size and generation size, a surrogate model of the time-consuming CFD solver is preferred. In this article, an artificial neural network is constructed as the surrogate model to give a quicker performance prediction.

The configuration of the network has one input layer, two hidden layers, and one output layer, as shown in Figure 8. The number of nodes in the input layer equals the number of design variables, and that of each hidden layers is set as 18. Each optimization objectives or constrains has its own artificial neural network, and it serves as the output node in the output layer. Nodes from the current layer form an input vector, which are connected to the next layer through a connection weight matrix. Nodes from the next layer then perform the summation of the weighted inputs and bias to form a scalar output. The learning process of the artificial neural network is driven by the back-propagation algorithm. It is able to find the best connection weight matrices and biases that produce the most accurate prediction results regarding the performance database within 100,000 iterations.

Optimization requirements

The optimization requirements for high performance transonic centrifugal compressors are increasing the compressor efficiency at the design speed while maintaining similar level of the operating range. Therefore, a multi-point optimization regarding the near surge, peak efficiency, and near choke points of the datum
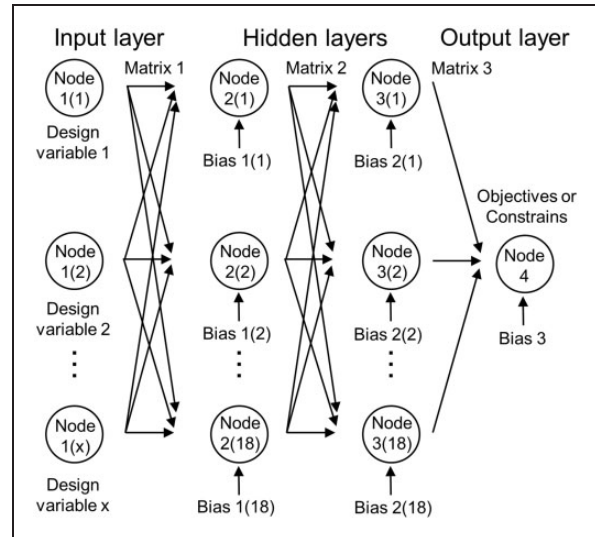

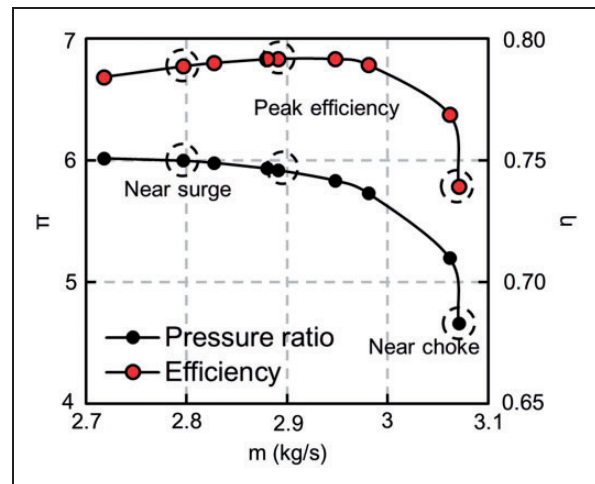**Figure 8.** Schematics of the artificial neural network.

Figure 9. Optimized multi-point illustration.

compressor is needed, as illustrated in Figure 9. During optimization loops, backpressures of the investigated points are kept the same as that of the datum case for CFD predictions.

Objectives and constrains of the optimization are listed as follows:

Objective 1: to maximize the isentropic efficiency at peak efficiency point.

$$\text{Max } \eta_p \tag{1}$$

Objective 2: to maximize the isentropic efficiency at near surge efficiency point.

$$\text{Max } \eta_s \tag{2}$$

Constraint 1: to penalize a significant reduction in the <mark>choke mass.</mark>

Please replace "choke mass" with "choke mass flow rate"

$$m_c \geqslant 0.99 m_{c,dat} \tag{3}$$

Through objective 1 and 2, the optimized design is expected to have higher efficiency at broad range of the design speed. The demand for maintaining similar level of the operating range can be reached by objective 2 and constraint 1. On the one hand, because cases that cannot reach convergence at the near surge condition will be removed from the database, final optimized design will still stably operate at the datum near surge condition and thus no significant reduction in the surge margin is expected. On the other hand, when constraining the lower bound of the choke mass flow rate by 99% of that of the datum case, no significant reduction of the choke mass flow rate will occur as well. Therefore, the optimized design will have a similar or even broader operating range compared to that of the datum case.

Genetic algorithm

The genetic algorithm mimics the biological evolution to produce an optimized solution to a given problem. At first, an initial population is generated and their performances are predicted by the surrogate model. After competition based on the performance, weak individuals will die out and stronger ones survive to bear offspring through crossover and mutation. In particular, the best individual of each generation will be directly transmitted to the next generation. After several generations of competence and selection, the reproduction loop converges, and the performance of the best result will be verified by the CFD solver and be updated in the database. In this article, the population size of each generation is set to be 50 and the generation size is set to be 100. The optimization loop is considered to be converged when it produces consistent results for over 20 iterations.

Sensitivity analysis

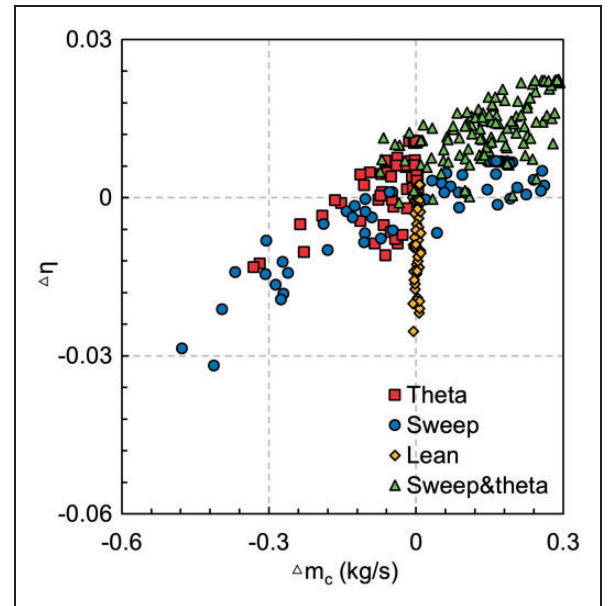### Comparison between camber curves, sweep, and lean

The first round of optimization investigates the blade camber curves, the sweep feature, and the lean feature individually. Sensitivity of different variable groups to objectives and constraints has been discussed first to guide the second optimization round that generates the truly optimized design.

Figure 10 presents performances of all design cases whose performance are predicted by CFD. The ordinate and the abscissa are defined as follows

$$\mark{\Delta \eta = \frac{1}{2}\eta_{p,opt} - \eta_{p,dat} + \eta_{s,opt} - \eta_{s,dat}} \tag{4}$$

Please add "()". The right hand side should be like the format: "1/2 (A-B+C-D)"

$$\Delta m_{c,opt} - m_{c,dat} \tag{5}$$

The variation range of performance is summarized in Table 5. For the variable group of camber curve theta angles, it has the largest potential in efficiency improvement by 1.1%, and the best efficiency case has nearly the same choke mass flow rate with the datum

Figure 10. Comparison of effects of camber curves, sweep, and lean on the performance.

Table 5. Variation range of the performance.

Variables	$\Delta \eta$ range	$\Delta m_c/m_c$ range
Theta	−1.3% to +1.1%	−10.8% to +0.1%
Sweep	−3.2% to +0.7%	−15.6% to +8.6%
Lean	−2.5% to +0.2%	−0.2% to +0.3%
Sweep&theta	0% to +2.2%	−2.4% to +9.6%

one. For the variable group of sweep, it has the largest variation range in both the efficiency and the choke mass flow rate. The best case of group sweep increases the efficiency by 0.7%, which also has higher choke mass flow than the datum design. For the variable group of lean, it has comparatively limited effect on the efficiency improvement and the choke mass flow rate, which is within 0.2% and 0.5%, respectively. Although little efficiency gain was obtained by optimizing lean feature, it still has the potential to reduce impeller stress levels by redistributing stresses on both pressure side and suction side of blades. Such potentials can be evaluated through multidisciplinary optimizations in future researches.

In the second round of optimization, the most potential variable groups, namely camber curve theta angles and sweep, have been considered together to achieve a truly optimized design. Parameters of the best case in former optimizations have been combined together as the optimization base case, and the variation range of all variables has been kept the same as shown in Table 2. Performances of all cases in the second round design cases have also been shown in Figure 10 and Table 5. It is surprising to find that the efficiency improvement by camber curves and sweep can be added up, and the best case increases the efficiency by 2.2% with an increased choke mass flow rate. Such result indicates that the mechanisms of the efficiency improvement for the two variable groups may be different.

Parametric study of camber curves

To investigate the effect of each design variables of blade camber curves, their Pareto fronts are presented

in Figure 11. From Figure 11(a), it is generally concluded that the efficiency front of the upstream control point at shroud is steeper than that of the downstream control point at hub, which indicates the efficiency is more sensitive to the front part of the shroud section. In Figure 11(b), the choke mass flow rate fronts of all cases are much similar to each other, which is because all design variables have equal influence to the throat area and thus the choke mass flow rate.

Parametric study of sweep

Pareto fronts of sweep variables are presented in Figure 12. In Figure 12(a), it can be seen that the control points near endwalls (SA and S1) are more influential than that near mid-span (S2 and S3), where the efficiency fronts are much steeper. The efficiency is found to increase with the enlarged forward sweep in the variation range, and the best case occurs near 8 degrees. For the choke mass flow rate presented in Figure 12(b), SA and S1 also show higher influence. When enlarging the forward sweep, the throat area increases by turning the throat more normal to the axial direction, which results in the increased choke mass flow rate.

Parametric study of lean

Pareto fronts of lean variables are presented in Figure 13. From the efficiency fronts in Figure 13(a), it is illustrated that control points near endwalls (L1 and L4) are more influential in changing the efficiency than that near mid-span (L2 and L3). In Figure 13(b),
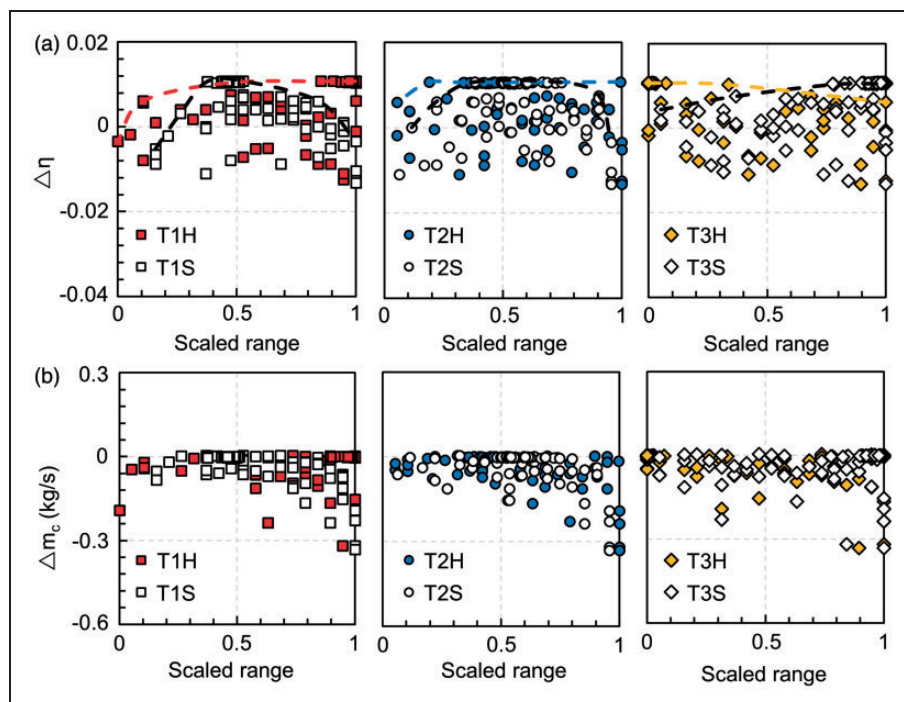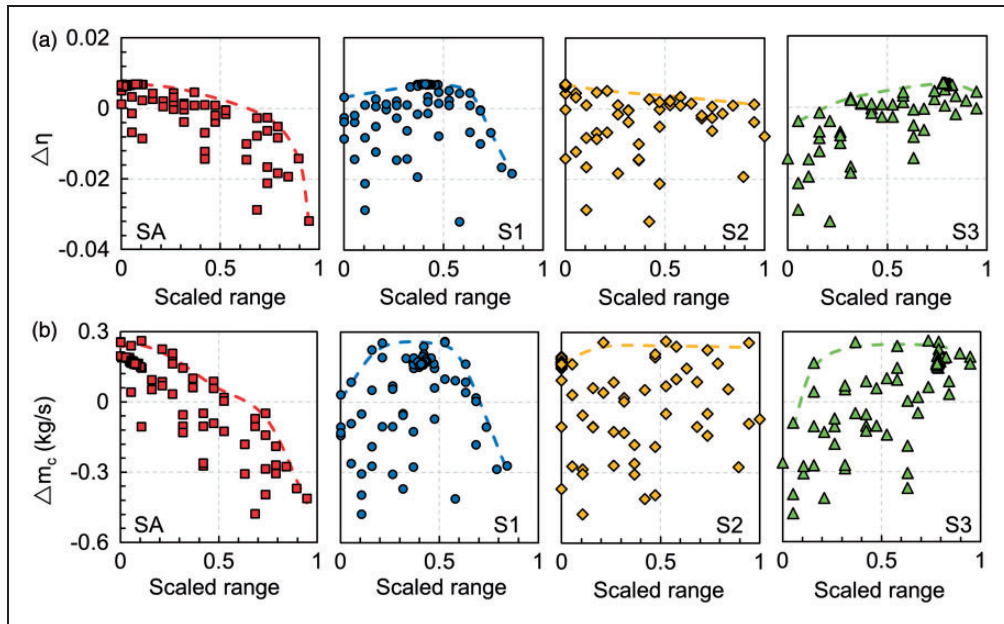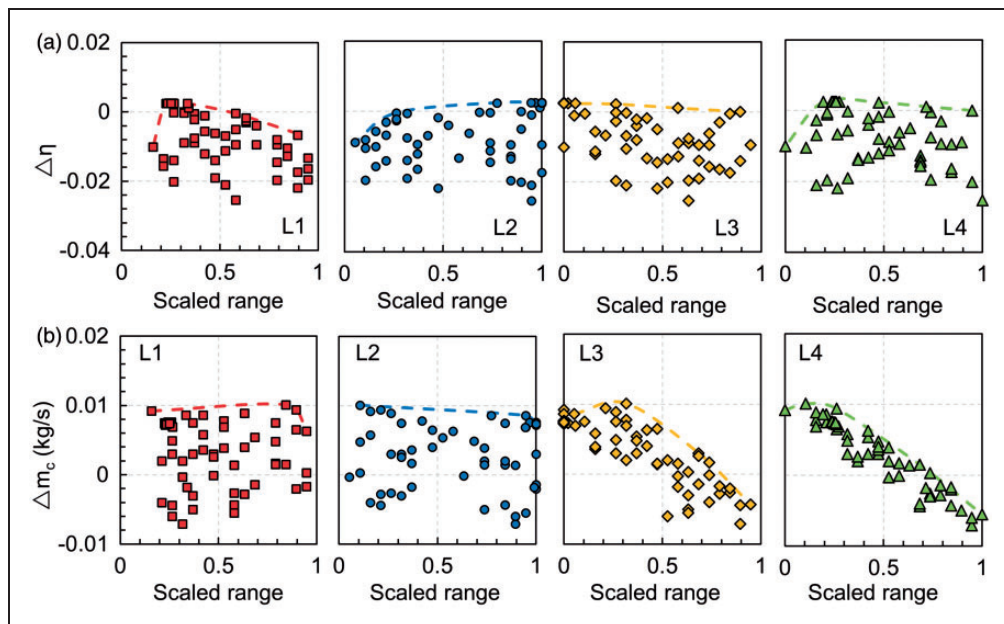

Figure 11. Pareto fronts of camber curves variables.

Figure 12. Pareto fronts of sweep variables.

Figure 13. Pareto fronts of lean variables.

although lean has relatively low influence on the choke mass flow rate compared to other variable groups, a linear trend can be observed in the result of L3 and L4. When leaning the blade to the rotating direction, the choke mass flow rate tends to be decreased by about 0.1% of the datum value per degree of leaning angle, which is in consistence with the result in another transonic centrifugal compressor case.[15]

Analysis of optimized cases

In this section, the optimized theta angles of camber curves case, the optimized sweep case, and the optimized sweep and theta angles case will be analyzed in detail. The aforementioned three cases will be abbreviated as the theta case, the sweep case, and the sweep&theta case, respectively for convenience.

Geometry comparison

Comparison of the geometries between the datum and optimized cases is presented in Figure 14. For the sweep case, it is generally forward swept with an S-shape leading edge. For the theta case, the main difference occurs at the pressure surface of the hub section, where an end-bend feature can be captured.
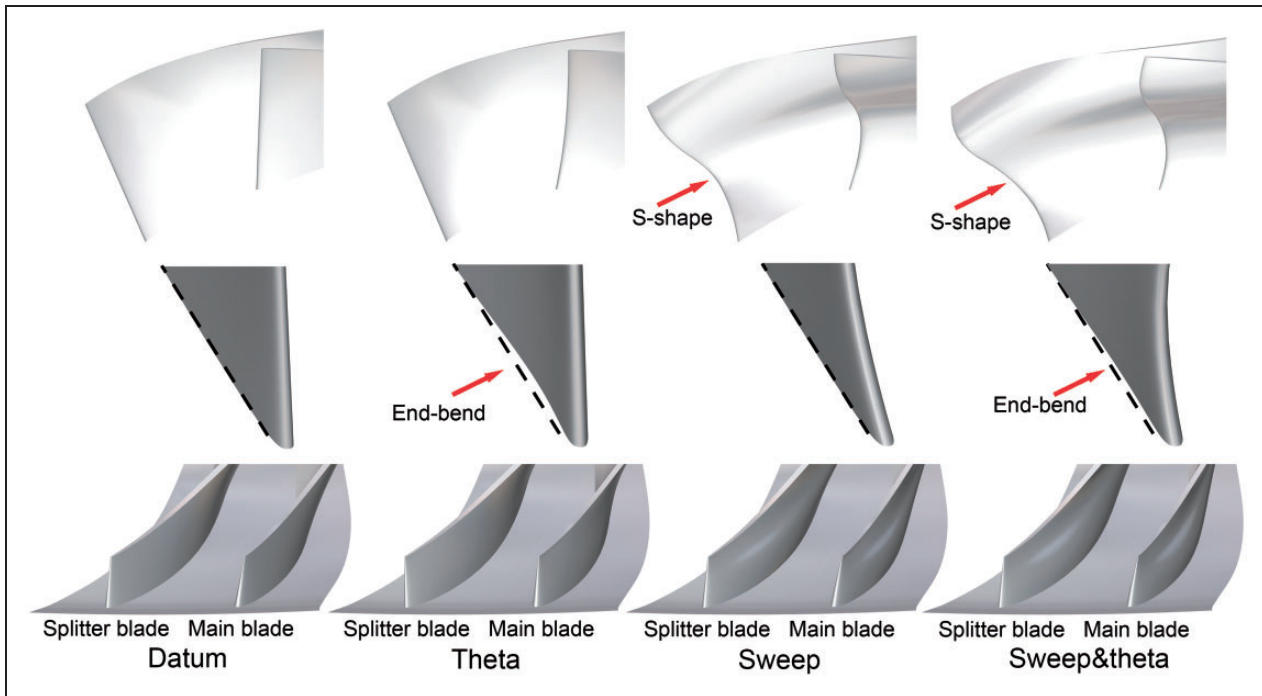
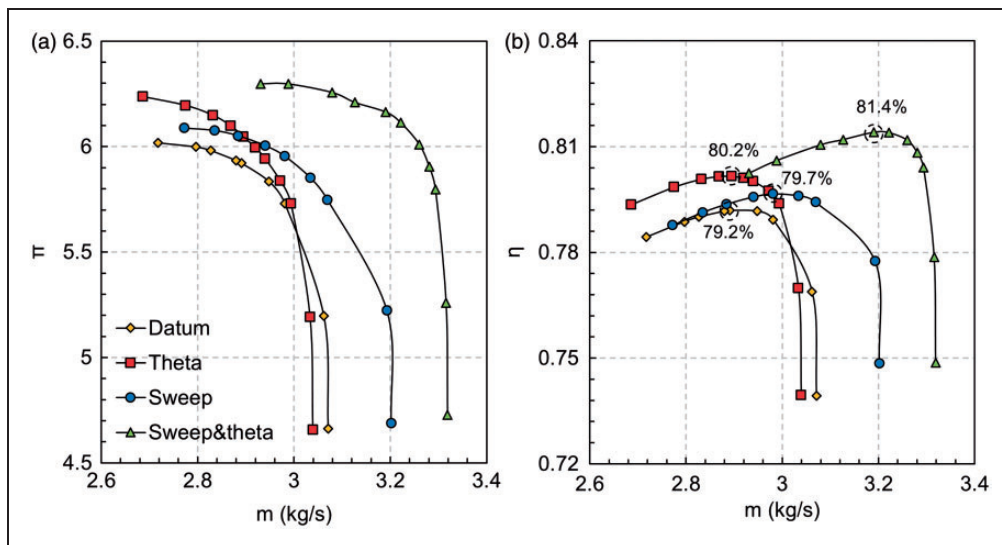**Figure 14.** Geometry comparison between datum and optimized cases.

Figure 15. Performance comparison at design speed between datum and optimized cases: (a) total pressure ratio and (b) isentropic efficiency.

When combining both the sweep and camber curves into optimization, the best geometry presents a combination of both the S-shape leading edge and the end-bend feature with only small modifications in both features. Since geometry changes by varying sweep and camber curves focus on the front part of the impeller, no obvious change is obtained near the impeller trailing edge.

Performance comparison

Comparison of the design speed performances between the datum and optimized cases is presented in Figure 15. From Figure 15(a), it is noticed that all optimized cases have a higher pressure ratio at the whole operating range than the datum case, and the increase in the peak pressure ratio of the theta case, the sweep case, and the sweep&theta case is 3.6%, 1.2%, and 4.6%, respectively. The pressure ratio is decided by the isentropic efficiency and the work input, as follows

$$\pi = \left[\left(\frac{T_{04}}{T_{01}} - 1 \right) \eta + 1 \right]^{\frac{\gamma}{\gamma-1}} \quad (6)$$

Because modifications of optimized cases mainly occur in the front part of the impeller, the change of the work input through a change in the exit blade angle or the slip factor is limited. Therefore, the increase in isentropic efficiency is believed to be the main cause for the pressure ratio increase. It is confirmed in Figure 15(b) that all optimized cases also show higher isentropic efficiency at the whole operating range, and the increase in the peak efficiency is 1.0%, 0.5%, and 2.2% for the theta case, the sweep case, and the sweep&theta, respectively.

Considering the constraints on choke mass flow rate, it can be seen in Figure 15 that the choke mass flow rate of the theta case, the sweep case, and the sweep&theta case has been varied by −1.0%, +4.3%, and +8.1%, respectively, which agrees with the optimization requirement. The surge mass flow rate has also been changed in a similar trend to that of the choke mass flow rate. Considering the definition of the SFR

$$SFR = \left(1 - \frac{m_s}{m_c}\right) \times 100\% \qquad (7)$$

The SFR of the aforementioned optimized cases is calculated to be 13.2%, 15.5%, and 13.2%, respectively, which share the similar level of 13.0% of the datum case.

For the purpose of understanding the efficiency improvement in detail, the parameter efficiency deviation ($\Delta\eta$) is applied to investigate the loss reduction process, as defined as follows

$$\Delta\eta(M) = \left(\frac{T_{02}\Delta s(M)}{\Delta h_{02}}\right)\Big|_{opt}^{dat} \qquad (8)$$

$$\Delta\eta(N) = \left(\frac{T_{02}\Delta s(N)}{\Delta h_{02}}\right)\Big|_{opt}^{dat} \qquad (9)$$

where M and N is corrected streamwise and spanwise coordinate from 0 to 1 (inlet to exit and hub to shroud) respectively, $\Delta s(M)$ is mass-averaged entropy rise of a cross-section cut at certain streamwise position, and $\Delta s(N)$ is pitch-averaged entropy rise at a certain spanwise position of a cross-section cut. The increase of $\Delta\eta$ along the M direction represents loss reduction at corresponding location, and a positive value of $\Delta\eta$ along spanwise direction represents a higher efficiency at corresponding location.

The $\Delta\eta$ distribution of optimized cases along streamwise direction is shown in Figure 16. It is obviously seen that the effect of optimized theta angles on the loss reduction mainly occurs at the front part before Section I, which locates near the leading edge of splitters. On the contrary, the performance of the sweep case gets worse at first before Section I, and then gradually recovers before impeller exit. At the vaneless diffuser downstream impeller exit, its performance has also been improved. For the
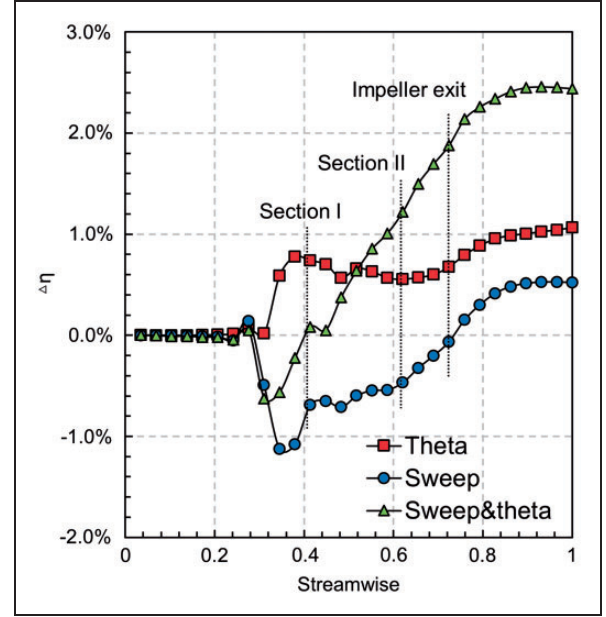
Figure 16. Efficiency deviation distribution along streamwise direction at peak efficiency point.
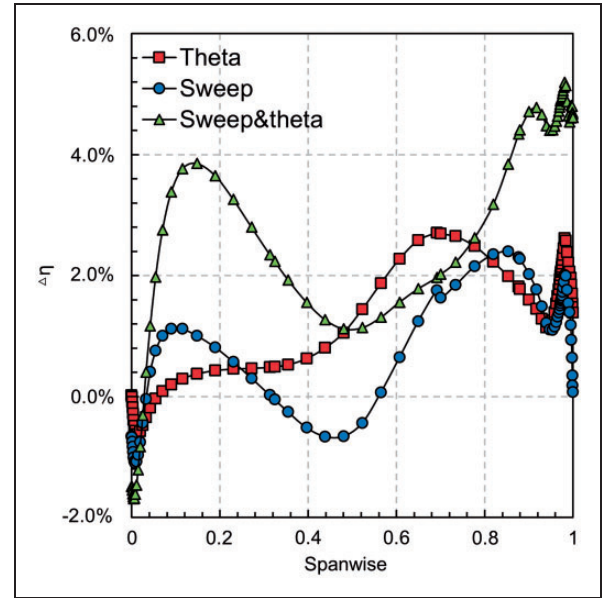
Figure 17. Efficiency deviation distribution along spanwise direction at impeller exit at peak efficiency point.

sweep&theta case, it is surprising to find that its loss reduction pattern combines both of the theta case and the sweep case. Because the performance improvement of the theta case and the sweep case occurs at different regions, such improvements can be added up when optimizing both theta angles of camber curves and the sweep feature.

The pitch-averaged $\Delta\eta$ distribution of optimized cases along spanwise direction at impeller exit is illustrated in Figure 17. The theta case shows performance improvement mainly from mid to upper spans, while the sweep case increases efficiency near hub and shroud spans. The sweep&theta case combines both

the theta case and the sweep case together, resulting in the performance improvement at all spans.

Flow mechanisms

To find the flow mechanisms behind the performance improvement of optimized cases, the shock wave near impeller leading edges and the jet-wake pattern near impeller trailing edges have been examined.

To exam the change in shock waves, Figure 18 presents the relative Mach number contour of the main blade and the splitter suction surface, respectively. For the theta case, it is obvious that the strength of the shock wave from mid to upper spans of the main blade has been significantly weakened, where the local relative Mach number is much lower than the datum case. The decreased shock strength will lead to a reduction in shock losses, which corresponds to the improved efficiency at Section I in Figure 16. It is also noticed that the high Mach number region near the tip of the splitter suction surface has been suppressed, which relieves the unnecessary accelerating-decelerating process and contributes to less loss. For the sweep case, the shock strength of the main blade slightly increases and thus leads to the increased shock loss. Moreover, the tip shock front has been moved more upstream, which will result in a much severe shock-boundary layer interaction and thus higher loss. As a result, the efficiency drops at Section I in Figure 16. In the middle part of the passage, the sweep case not only blends the two separated high Mach region near the main blade into a same region, but also

suppresses the high Mach region at suction surface of the splitter. These effects contribute to the higher efficiency of sweep between Section I and impeller exit due to the relief of the unnecessary accelerating-decelerating process, as shown in Figure 16. The sweep&theta case basically combines both effects of the theta case and the sweep case together. Therefore, the decreased shock strength and the forward-swept shock front lead to nearly no change in efficiency at Section I, while the blended high Mach region of the main blade and the reduced high Mach region of the splitter result in the efficiency increase between Section I and impeller exit, as presented in Figure 16.

Figure 19 presents the relative Mach number contour at Section II, which compares the change in the jet-wake pattern between the datum and optimized cases. In all optimized cases, it is generally seen that the wake region in the channel between the main blade pressure surface and the splitter suction surface (right channel in Figure 19) has been significantly suppressed, but the wake region in the other channel has been slightly enhanced. The reduced wake region will not only decrease the wake friction loss inside the blade passage between Section I and impeller exit, but also lead to an improved flow uniformity and thus a reduction in mixing loss downstream impeller exit. Because the sweep&theta case has the most reduced wake region regarding both channels, its efficiency increases the most between Section I and impeller exit and downstream impeller exit in Figure 16. The increased efficiency by suppressed
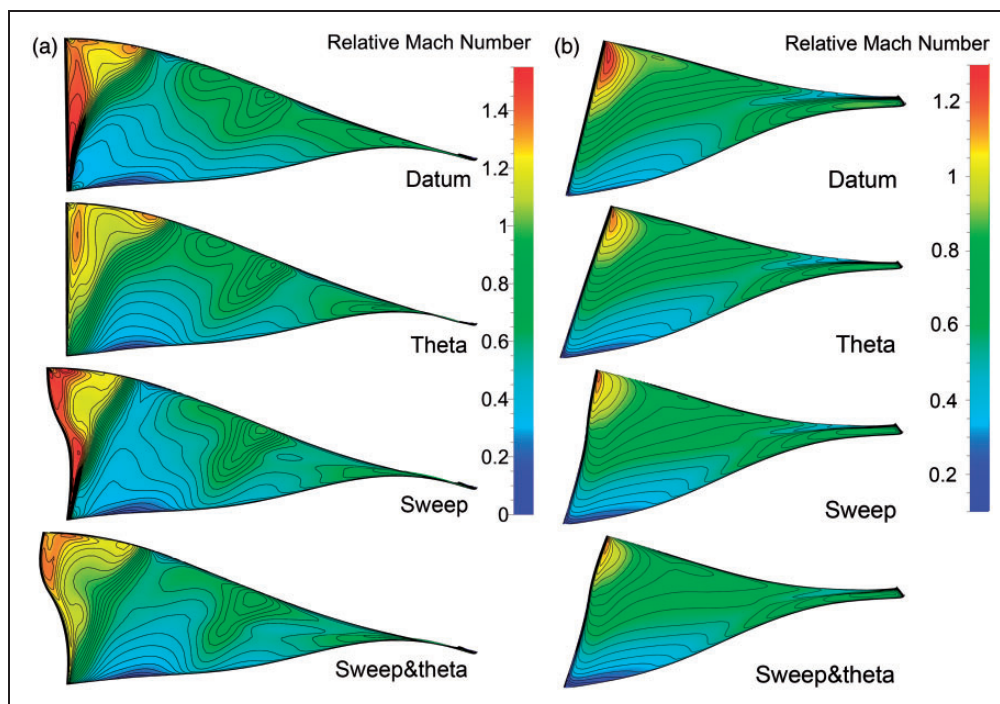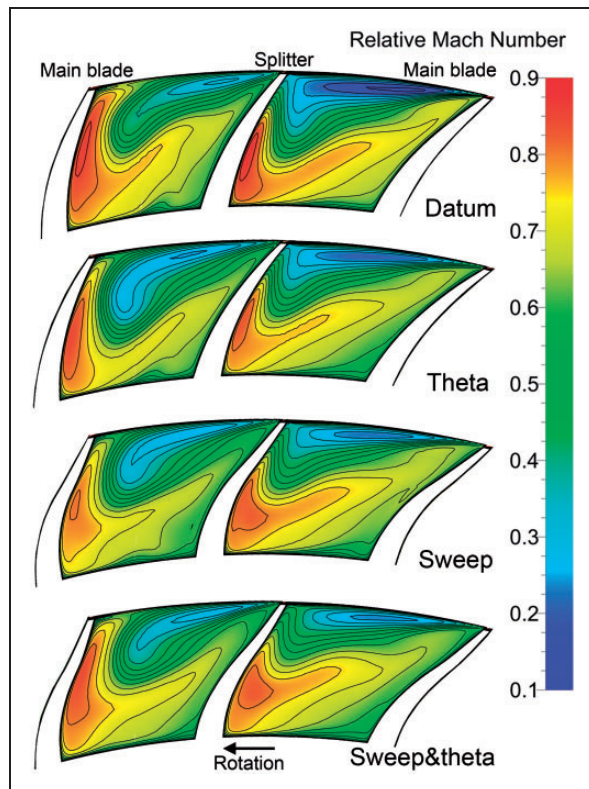

Figure 18. Relative Mach number contour of the (a) main blade and (b) splitter suction surface at peak efficiency point.

Figure 19. Relative Mach number contour at Section II at peak efficiency point.

wake region occurs from mid to upper spans, which also corresponds to the results in Figure 17.

Concluding remarks

In this article, evaluation of the aerodynamic potential of three-dimensional features in a transonic centrifugal compressor has been made. The blade camber curves, the sweep feature, and the lean feature have been optimized through a multi-point and multi-objective optimization system, aiming to improve the efficiency while maintaining similar level of the SFR. Several conclusions can be drawn as follows:

1. Complex three-dimensional features have significant potential to improve the performance of transonic centrifugal compressors. The blade camber curves and the sweep feature have great influences in increasing the impeller efficiency and its flow capacity, while the lean feature shows limited aerodynamic potentials. Because the loss reduction mechanisms of optimizing camber curves and sweep are different, the efficiency improvement by both variable groups can be added up. The best result of optimizing both camber curves and sweep shows end-bend and S-shape leading edge patterns, and its peak efficiency and choke mass flow rate has been increased by 2.2% and 8.1%, respectively.

2. When optimizing the camber curves, the best result shows an end-bend feature at the front of the hub section, and the efficiency has been improved by 1.0% due to the lowered shock strength. The design at front part of the shroud section is most sensitive to impeller performances.
3. When optimizing the sweep feature, the best result presents an S-shape leading edge and a forward sweep feature. The efficiency increases by 0.5% because of the reduced wake region. The sweep design near endwalls is most important to impeller performances.
4. When optimizing the lean feature, the optimized lean feature only improves the efficiency by 0.2%, which shows its relatively low potential. The lean design near endwall is most influential to impeller performances. In future research, multidisciplinary optimizations are needed to evaluate its potential in decreasing impeller stress levels without significant loss in aerodynamic performances.

References

1. Krain H. Review of centrifugal compressor's application and development. *J Turbomach* 2005; 127: 25–34.
2. Rodgers C. Flow ranges of 8.0: 1 pressure ratio centrifugal compressors for aviation applications. ASME paper GT2005-68041, 2005.
3. Rodgers C. The efficiencies of single-stage centrifugal compressors for aircraft applications. ASME paper 91-GT-77, 1991.
4. Higashimori H, Hasagawa K, Sumida K, et al. Detailed flow study of Mach number 1.6 high transonic flow with a shock wave in a pressure ratio 11 centrifugal compressor impeller. *J Turbomach* 2004; 126: 473–481.
5. Ibaraki S, Matsuo T, Kuma H, et al. Aerodynamics of a transonic centrifugal compressor impeller. *J Turbomach* 2003; 125: 346–351.
6. Lohmberg A, Casey M and Ammann S. Transonic radial compressor inlet design. *Proc Inst Mech Eng A J Power Energy* 2003; 217: 367–374.
7. Eisenlohr G, Krain H, Richter FA, et al. Investigations of the flow through a high pressure ratio centrifugal impeller. ASME paper GT-2002-30394, 2002.
8. Li Z, Zheng X, Liu Y, et al. The effect of end wall boundary layer on matching and corresponding flow control technique for multistage axial compressor. *Proc Inst Mech Eng G J Aerosp Eng* 2015; 0954410015621928.

9. Vad J. Aerodynamic effects of blade sweep and skew in low-speed axial flow rotors at the design flow rate: an overview. *Proc Inst Mech Eng A J Power Energy* 2008; 222: 69–85.

10. Vad J. Forward blade sweep applied to low-speed axial fan rotors of controlled vortex design: an overview. *J Eng Gas Turb Power* 2013; 135: 012601.

11. Hazby HR and Xu L. Effects of leading edge sweep on the performance of a centrifugal impeller. ISABE paper ISABE-200701225, 2007.

12. Denton JD and Xu L. The exploitation of three-dimensional flow in turbomachinery design. *Proc Inst Mech Eng C J Mech Eng Sci* 1998; 213: 125–137.

13. Ono H, Senoo S, Kudo T, et al. The effects of the tangential leans for the last stage nozzles of steam turbine. ASME paper GT2013-95827, 2013.

14. Rosic B and Xu L. Blade lean and shroud leakage flows in low aspect ratio turbines. *J Turbomach* 2012; 134: 031003.

15. He X and Zheng X. Mechanisms of lean on the performance of transonic centrifugal compressor impellers. *J Propul Power* 2016; 32: 1220–1229.

16. Lian Y, Oyama A and Liou MS. Progress in design optimization using evolutionary algorithms for aerodynamic problems. *Prog Aerosp Sci* 2010; 46: 199–223.

17. Okui H, Verstraete T, Van den Braembussche RA, et al. Three-dimensional design and optimization of a transonic rotor in axial flow compressors. *J Turbomach* 2013; 135: 031009.

18. Lu H, Li Q and Pan T. Optimization of cantilevered stators in an industrial multistage compressor to improve efficiency. *Energy* 2016; 106: 590–601.

19. Verstraete T, Alsalihi Z and Van den Braembussche RA. Multidisciplinary optimization of a radial compressor for microgas turbine applications. *J Turbomach* 2010; 132: 031004.

20. Ju Y, Zhang C and Chi X. Optimization of centrifugal impellers for uniform discharge flow and wide operating range. *J Propul Power* 2012; 28: 888–899.

21. Fine Design3D v8.9 user manual. Brussels: NUMECA International, 2013. **[AQ3]**.

22. Fine Turbo v9.0 user manual. Brussels: NUMECA International, 2013. **[AQ4]**.

23. Spalart P and Allmaras S. A one-equation turbulence model for aerodynamic flows. AIAA paper 92-0439, 1992.

24. Krain H, Hoffmann B and Pak H. Aerodynamics of a centrifugal compressor impeller with transonic inlet conditions. ASME paper 95-GT-79, 1995.

25. Yi W, Chen Z and Ji L. Numerical studies on application of blended blade and endwall technique on transonic centrifugal compressor. ASME paper GT2014-26660, 2014.

26. Mangani L, Casartelli E and Mauri S. Assessment of various turbulence models in a high pressure ratio centrifugal compressor with an object oriented CFD code. *J Turbomach* 2012; 134: 061033.

27. Hazby H, Woods I, Casey M, et al. Effects of blade deformation on the performance of a high flow coefficient mixed flow impeller. *J Turbomach* 2015; 137: 121005.

28. Sun Z, Tan C and Zhang D. Flow field structures of the impeller backside cavity and its influences on the centrifugal compressor. ASME paper GT2009-59879, 2009.

29. Gu L, Zemp A and Abhari RS. Numerical study of the heat transfer effect on a centrifugal compressor performance. *Proc Inst Mech Eng C J Mech Eng Sci* 2015; 229: 2207–2220.

30. Benichou E and Trebinjac I. Comparison of steady and unsteady flows in a transonic radial vaned diffuser. *J Turbomach* 2016; 138: 121002.

Appendix

Notation

b	blade height
h	enthalpy
L1–L3	control points of lean
m	mass flow rate
m'	normalized distance along the meridional curve
M	corrected distance in the streamwise direction
n	shaft speed
N	corrected distance in the spanwise direction
r	radius
s	entropy
SA	sweep angle
SFR	stable flow range
S1–S3	control points of sweep
T_0	total temperature
T1H–T3H	control points of hub camber curve
T1S–T3S	control points of shroud camber curve
y^+	normalized wall distance
Z	number of blades
β	blade angle
γ	ratio of specific heat capacities
η	isentropic efficiency
θ	theta angle
π	total-to-total pressure ratio

Subscripts

1	impeller inlet
2	impeller exit
4	diffuser exit
c	near choke condition
d	design condition
dat	datum case
h	hub section
opt	case generated in optimization
p	peak efficiency condition
s	near surge condition
t	tip section

The order of Refs. 21-24 has been checked. The current form is OK.

Refs 21 and 22 are books. The author group is "NUMECA International", and the publication place is "Brussels, Belgium".